Composites of AISI 316L stainless steel and nanocrystalline Ti-B-C ceramic powders

Slawomir M. Kaczmarek[1*], Tomasz Bodziony[1], Vinh H. Tran[2], Piotr Figiel[3], Anna Biedunkiewicz[3], Grzegorz Leniec[1]

[1]*Institute of Physics, West Pomeranian University of Technology, Al. Piastów 17, 70-310 Szczecin, Poland*
[2]*Institute of Low Temperatures and Structural Research, 2 Okólna str., 50-422 Wrocław, Poland*
[3]*Institute of Materials Science and Engineering, West Pomeranian University of Technology, Al. Piastów 17, 70-310 Szczecin, Poland*

*Corresponding author

DOI: 10.5185/amlett.2018.2161
www.vbripress.com/aml

Abstract

Series of nanocrystalline and TiC, TiB_2, and B_4C powders as dopants (3%-20%) embedded in an AISI 316L austenitic steel have been prepared and investigated by ferromagnetic resonance and magnetic measurements. The homogeneous composites with the dopants up to x = 7 vol. % exhibit superparamagnetic properties, characterized by bifurcation between the field-cooled $M_{FC}(T)$ and zero-field cooled $M_{ZFC}(T)$ magnetization below T_{ir} and a maximum at T_{max} in low-field $M_{ZFC}(T)$ curves. We found that the T_{ir} and T_{max} values depend proportionally on the dopant concentrations x. The magnetization measurements in fields above 1000 Oe suggested an induced phase transition from superparamagnetic state to ferromagnetic one but presumably without long-range magnetic correlation. An analysis of magnetic anisotropic energy barrier distributions implied that different sizes and compositional types of dopants may contribute to the superparamagnetic relaxation process. The results demonstrate the possibility of obtaining new steel-based materials with desired properties and potential applications as combining magnetic and mechanical advantages.

Keywords: Nanocrystalline, Ti-B-C, FMR, magnetic susceptibility.

Introduction

Mechanical or magnetic properties of the 316L austenitic steel have been investigated for many years [1]. The 316L austenitic steel contains the following elements: iron 72%, chromium 16-18%, nickel 10-14%, molybdenum 2 – 3 %, manganese 2% and trace amounts of carbon (<0.08%), nitrogen, manganese, phosphorus, sulfur, silicon (information based on Product Data Sheet 316/316L Stainless Steel) [2]. Austenitic steel type 316L is a special, extra-low carbon version of austenitic chromium-nickel stainless steel containing molybdenum. The steel belongs to so-called 'non - magnetic' austenitic stainless steel [2, 3]. In general, the 316L austenitic steel exhibits weak magnetic properties. However, a small but stable ferromagnetic (FM) component is always present and the effects of exchange anisotropy are shown [1]. The exchange bias behavior was observed between strain-induced ferromagnetic FM martensite and antiferromagnetic (AFM) austenitic phase in 316LN stainless steel at a temperature below 30 K [3]. Moreover, magnetic properties of AISI 316L steel strongly depend on carbon concentration. It was shown, that samples with low carbon content, less than 0.13%, show typical magnetization (M(T)) dependence decreasing with increasing temperature, while samples with carbon content higher than 0.13% reveal long-range antiferromagnetic interactions. M(T) dependence increases with increasing temperature [4]. Thus, it is expected that - an admixture of magnetic ions, such as - Ti-B-C system will modify magnetic properties of the steel to match the required multifunctional application.

Nanostructure materials often have unique chemical, structural, electrical, and magnetic properties [5–8] with potential applications including information storage [9], color imaging, bioprocessing, magnetic refrigeration [10,11], and ferrofluids [12,13]. Nanostructured materials exhibit a unique type of disorder. A study of austenitic composites of AISI 316L steels doped with nanocrystalline and TiC, TiB_2, and B_4C is currently of interest [14]. Titanium carbide (TiC_x) and titanium nitride (TiN_x) [15-18] are very important technological materials because being refractory materials they have gained much attention due to their extraordinary hardness. Titanium compounds are used in cutting tools and high-temperature alloys for a wide range of engineering applications. These compounds are the most intensively studied, both experimentally and theoretically, with regard to their physical properties. Titanium diboride (TiB_2) has attracted great interest due to its excellent

mechanical properties, chemical resistance and good thermal and electrical conductivities. Fracture and wear resistance of TiC–TiB_2 composites obtained from TiB_2 and TiC powders is higher than that of single TiB_2 and TiC phases. For this reason, these composites are used for manufacturing metal-matrix composites (MMCs) and cutting tools as well as heat exchanger elements and combustion engine elements [18, 19]. Metal-matrix composites are generally made of a ductile matrix and a hard ceramic material which serves as reinforcement. Iron-based composites containing TiC exhibit the toughness and machinability associated with conventional alloy steels but exceeds them in hardness and wear resistance. The addition of titanium diboride (TiB_2) to metal matrices has also been observed to greatly increase stiffness, besides hardness and wear resistance [20, 21].

Boron carbide (B_4C) is one of the hardest materials ever known, ranked third after diamond and cubic boron nitride (c-BN). It has ultrahigh hardness, high wear and impact resistance and low specific weight, good chemical stability. Boron carbide (B_4C) can be used as a ceramic armor, an ideal neutron moderator and screening material in the nuclear industry because it has high neutron absorption coefficient [22–25]. B_4C is also considered to be interesting due to its high stability in corrosive solutions and good electrical conductivity [26].

The previous studies of nanocrystalline powders suggest that mainly TiB_2, TiC and B_4C compounds are presented in the Ti–B–C systems doped to AISI 316L austenitic steel [8, 9, 27-28]. Titanium diboride (TiB_2) and core-shell type TiC/C are characterized by many crystallographic and magnetic phases. These materials are widely studied because of their unusual properties including magnetic properties.

The paper deals with the study of nanocrystalline TiB_2, TiC and B_4C powders doped to AISI 316L austenitic steel, depending on the volumetric ratio of reinforcing phase. Composites with several concentrations (3, 5, 7, 10 and 20 vol.%) of Ti-B-C powders were characterized using X-ray diffraction (XRD) measurements and scanning electron microscope (SEM) investigation. The temperature dependence of the ferromagnetic resonance (FMR) spectra of the above samples was presented and discussed. Additionally, the MS measurements have been carried out and their results have been compared with FMR measurements. We will try check possibility of getting new, desired properties for specific applications of the 316L steel by suitable tuning of concentrations and sizes of dopants.

Experimental

Materials/ chemicals details

Five samples investigated in this work are numbered as 1, 2, 3, 4, 5, corresponding to doped concentrations of 3%, 5%, 7%, 10% and 20% vol. Ti-B-C system, respectively **(see Table 1)**.

Table 1. The compositions of the investigated samples 1, 2, 3, 4 and 5.

Sample	Ti-B-C system (% vol.)	Austenite steel 316L (% vol.)	Ceramics powders
1	3	97	TiC, TiB_2, B_4C
2	5	95	TiC, TiB_2, B_4C
3	7	93	TiC, TiB_2, B_4C
4	10	90	TiC, TiB_2, B_4C
5	20	80	TiC, TiB_2, B_4C

Material synthesis / reactions

The details of the preparation of the Ti-B-C system were previously described in [29]. The synthesis was carried out in two stages. At first, the precursor was obtained at the low-temperature stage, where nanocrystalline Ti-B-C powders were synthesized by a nonhydrolytic sol-gel method. Then, the ceramic phases were synthesized under argon atmosphere. In this system TiC, TiB_2 and B_4C nanocrystalline particles were obtained.

Average crystals size calculated from Scherrer equations [30] were the following 22, 62 and 98 nm for TiC, TiB_2, and B_4C respectively. The highest ratio of TiC phase with respect to TiB_2 and B_4C (71, 17 and 11% of particles cardinality) was obtained. The mixtures of nanocrystalline Ti-B-C powders and powder 316L (C<0.03%) austenitic steel were sintered using Selective Laser Melting (SLM) technique described in [14]. Manufactured samples were then cut, mounted on bakelite resin, grounded and polished according to the standard procedure.

The phase characterization of the investigated samples revealed that the addition of Ti-B-C nanopowders, as reinforcements to the steel matrix, has influenced the phase composition. The samples with Ti-B-C nanopowders up to 7 vol. % were found to be a homogeneous mixture consisting of (γ-Fe) and $Me_{23}(C, B)_6$ phases, where Me were Cr, Fe, and Mn. The content of the $Me_{23}(C, B)_6$ phase increases gradually with increasing Ti-B-C powders in the steel matrix **(Fig. 1a-c)**. Moreover, the XRD analysis has shown that the presence of TiC carbide may originate from the Ti-B-C powders. Furthermore, one recognizes that the intensity of the Bragg reflections of γ-Fe phase decreases with increasing α-Fe phase. The appearance of Fe_2B phase can be explained if we assumed that chemical reactions of Ti-B-C powder with the matrix material take a place since thermodynamic analysis has shown that the following reactions are likely to occur [34]:

$$B_4C + 8Fe = 4Fe_2B + C \quad (1)$$

$$2TiC + B_4C = 2TiB_2 + 3C \quad (2)$$

$$TiB_2 + 4Fe + C = 2Fe_2B + TiC \quad (3)$$

In isothermal and isobaric conditions, the change of free enthalpy ΔG of the system during the reactions (2) and (3) is negative in the temperature range 0 to 2000°C [13]. The lowest values of ΔG in this temperature range are achieved when the reaction (2) is dominant. This suggests that B_4C present in Ti-B-C powders was responsible for the formation of Fe_2B phase in the obtained composites.

Characterizations / device fabrications / response measurements

The SEM images of 20 vol. % Ti-B-C/316L composites are shown in **Fig. 2a**. The cross-sectional view of the polished surfaces reveals a complex morphology of the sample (left panel). On the magnified section (right panel) large Fe_2B grains surrounded by the steel matrix are visible. Fine Ti-B-C powder particles are located mainly between the grains of steel (γ-Fe, α-Fe phases) and Fe_2B phases. Typical HRTEM images of the TiC, TiB_2, and B_4C particles are shown in **Fig. 2b**. **Fig. 3** shows EDS element mapping for 20 vol. % Ti-B-C/316L composite to further elucidate the morphology. The distribution of elements reveals two regions, first rich in Cr and second one rich in Fe and Ni. The titanium (Ti, mainly TiC) is located in the zone between steel and Fe_2B. It can be concluded that the addition of Ti-B-C powders larger than 10 vol. % may lead to a precipitation of Cr, Fe and Ni-based phases in the steel matrix.

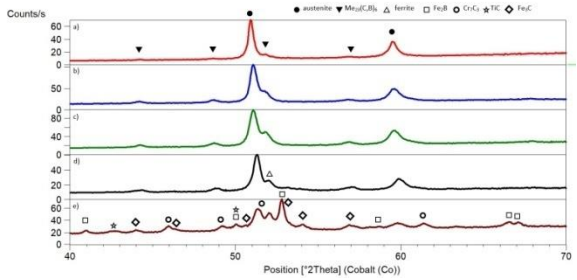

Fig. 1. XRD spectra of Ti-B-C/316L composites: sample 1 (3% vol. Ti-B-C), b) sample 2 (5% vol. Ti-B-C), c) sample 3 (7% vol. Ti-B-C), d) sample 4 (10% vol. Ti-B-C), e) sample 5 (20% vol. Ti-B-C).

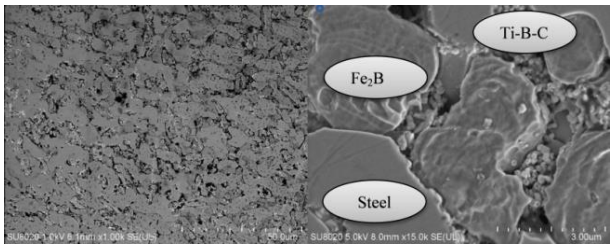

Fig. 2a. SEM images showing the characteristic morphologies of 20% vol. Ti-B-C system in 316L austenite steel (left panel) and enlarged fragment with description main crystallographic phases (right panel).

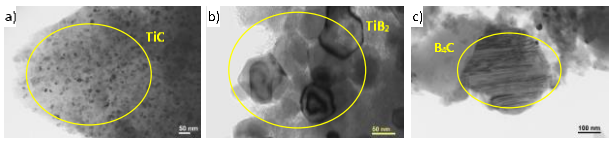

Fig. 2b. HRTEM images of the nanocrystals, respectively: (a) TiC, (b) TiB_2, c) B_4C.

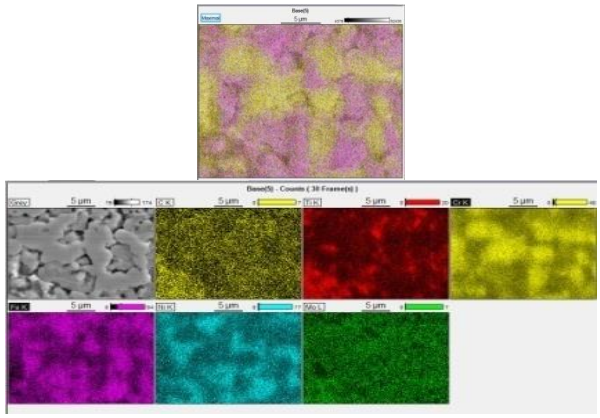

Fig. 3. EDS element mapping showing the distribution of major elements in 20% vol. Ti-B-C/316L composite.

The composite samples marked as Ti-B-C/316L were characterized by X-ray diffraction (XRD) using a PANalyticalX'Pert PRO X-ray powder diffractometer with CuKα radiation at 40 kV and 35 mA, applying a continuous scan mode. The microstructure was examined using Hitachi SU8020 Cold Field Emission SEM and JEOL JEM-1200EX TEM apparatus. Detection of Secondary Electrons (SE) at 15 kV accelerating voltage was used. Chemical composition was checked by EDX element maps using Thermo Fisher Scientific Noran 7 system.

FMR absorption measurements were carried out with a conventional X-band (ν = 9.43 GHz) Brucker E 500 spectrometer with 100 kHz magnetic field modulation. The measurements were performed in the temperature range from helium to room temperature with ΔT = 0.1 K stability using an Oxford cryogenic system.

M(T) measurements were carried out with a Quantum Design MPMS-7 SQUID magnetometer in the temperature range 4 - 300 K and in magnetic fields up to 10 kOe. Iso-field curves were collected in the zero-field-cooled (ZFC) and field cooled (FC) modes.

Results and discussion

FMR investigations

Fig. 4a shows the examples of FMR spectra of the samples 1-5 at two different temperatures: low temperature, about 10 K, and high temperature, about 240 K, for comparison. The asymmetries of the overlapped lines can be explained by assuming that the spectrum is a superposition of several separate resonance lines and so different magnetic centers. Moreover, due to the low concentration of carbon, free electrons contribution to FMR lineshape is expected to be present (Dyson like shape). It can be seen that asymmetries grow with the increase of the concentration of impurities. It should be noticed that sample 2 FMR spectrum behavior is different from that of other samples. FMR spectrum of sample 2 with 5% of Ti-B-C impurities is much more intense than the spectrum of sample 3 with 7% of the impurities in the low-temperature range.

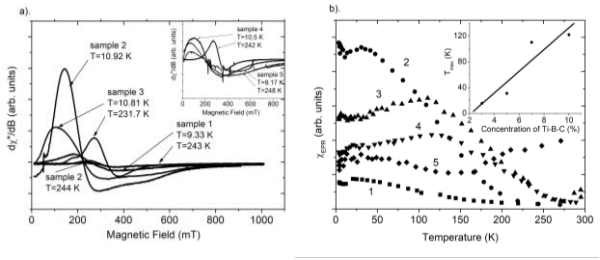

Fig. 4. (a) The comparison of FMR spectra of samples 1-5 at low ≈ 10 K and at ≈ 240 K temperature ranges; (b) The temperature dependences of the integrated intensity of the FMR spectra for samples 1-5. In the inset, T_{max} dependence v/s dopant concentration is presented.

Fig. 4b shows the temperature dependence of the integrated intensity of the FMR spectra of samples 1-5. In the inset, T_{max} linear dependence v/s dopant concentration up to ~10 % is presented. Similarly, as in the case of absorption, the integrated intensities of samples 2-5 are much higher than the one recorded for sample 1. Moreover, they decrease with increasing sample number from 2 to 5. The abnormally high integrated intensity of sample 2 (5% Ti-B-C) suggests that there exists a unique amount of impurity in steel in which magnetic interactions are extremely strong.

The integrated intensity was obtained either by numerical integration of the FMR absorption spectra or by double numerical integration of the first derivative spectrum usually registered by the EPR spectrometer. It is often named as FMR susceptibility. There are a few types of behavior of the susceptibility. Firstly, the susceptibility decreases with the increase of temperature from 4 K up to ~9 K. Secondly, it increases reaching its maximum at 15.77 K, 31.2 K, 110 K, 122.05 K, for samples 1-4, respectively (T_{max} in the inset of Fig. 4b). The susceptibility of sample 5 has no clear temperature maximum in the temperature range up to 300 K. The increase in the integral intensity of the EPR line at high temperatures region (above 150 K) suggests the dominance of EPR signals from the transition metal ions, for example, titanium, revealing also AFM interaction **(Fig. 5a)**. These maximal temperatures may be assigned to blocking temperatures, T_B. We suggest that superparamagnetic phase of nanoparticles is consistently responsible for a behavior observed by means of the FMR in the temperature range between ≈ 20 K and ≈ 240 K with the characteristic blocking temperature.

As one can see from **Fig. 4b**, T_{max} increase with increasing amount of dopant concentration. Above T_{max}, the susceptibility decreases with the increase of the temperature. However, this decrease is not homogeneous. It can be said that in each of the above temperature intervals different magnetic interaction dominate (due to Fe, Cr, and Ti). The susceptibility points are very well fitted by the Curie–Weiss curves in the low-temperature range from 4 K to 10 K and in the high-temperature range over T_{max}. Very similar behavior as susceptibility v/s temperature one can find for a product of integrated intensity and temperature v/s temperature, which can be a measure of magnetic momentum. It manifests in linear dependence of its temperature maximum v/s dopant concentration (T_{1max}). Moreover, in the temperature range up to T_{1max}, it increases while over T_{1max} decreases with increasing temperature. So, all of the investigated samples reveal a change in a kind of magnetic interactions from AFM-like at low temperatures to FM-like for temperatures higher than T_{1max}. Between 20 and 240 K superparamagnetic like interactions may be detected. In this temperature range, EPR lineshapes behave non-monotonically. They increase with increasing temperatures at low temperature and decrease exponentially for higher up to they reach minimum and further increase.

One can conclude that dependently on a temperature range, (anti)ferromagnetic and superparamagnetic interactions are present in Ti-B-C/316 L steel samples 1-5.

Low magnetic field properties

Fig. 5a shows the temperature dependencies of magnetization measured in a magnetic field of 10 Oe with FC and in ZFC modes for samples: 1, 2, 3 and austenitic steel 316L. At first, it is evident that the magnetic behavior of the austenitic steel 316L samples distinctly differs from the remaining samples. The magnetizations of the latter exhibit strong temperature dependencies, in contrary to that of the steel possessing magnetization practically temperature independent. Therefore, we may ascribe the presence of Ti-B-C nanoparticles in the steel matrix as the reason of anomalies observed in $M_{ZFC}(T)$ and $M_{FC}(T)$ curves of the doped samples.

In general, the magnetization curves of samples 1, 2 and 3 can be characterized by several substantial features: (i) A knee-like anomaly appears in the $M_{ZFC}(T)$ curves at about 20 K, (ii) The $M_{ZFC}(T)$ data do exhibit a broad maximum at T_{max}, (iii) The $M_{ZFC}(T)$ and $M_{FC}(T)$ curves are separated from each other below a characteristic irreversibility temperature T_{ir}, (iv) The magnetization values are samples dependent, and in the same manner as T_{max} and T_{ir} increase with increasing doped Ti-B-C contents. The findings (ii) and (iii) are typical superparamagnetic behavior, often observed in magnetic nanoparticles [31].

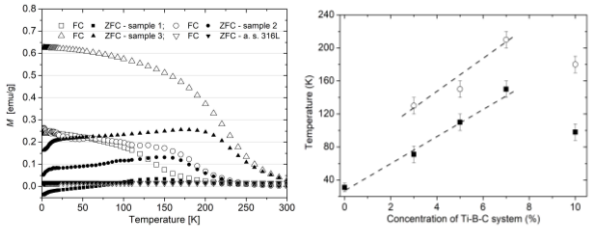

Fig. 5. (a). Magnetization measured with FC and ZFC modes for the samples 1, 2, 3 and austenitic steel 316L in an applied magnetic field of 10 Oe, (b). The temperature of separation and the temperature of a maximum of magnetization measured in ZFC modes versus concentration of Ti-B-C system in 316L austenitic steel in a magnetic field of 100 Oe, empty and full circles, respectively.

Obviously, a satisfactory explanation for the finding is obtained, if the superparamagnetic model [31-34] is applied. The physical mechanism behind this phenomenon leans on a competition of at least two processes: a rapid superparamagnetic relaxation of particle magnetic moments associated with magnetic anisotropy energy barriers and the thermal activation energy allowing flips of magnetic moments. When cooling samples in the zero magnetic field, the energy of each particle tends to the lowest value by the arrangement of the magnetic moment along its easy axis. Since the nanoparticles are randomly distributed, the total magnetization shows minimum value at low reachable temperatures. When the iso-field measurement is starting from this low temperature, the superparamagnetic relaxation occurs as a consequence of magnetic anisotropy energy. Thus the ZFC magnetization increases with increasing temperature. This situation will occur as long as the thermal energy becomes comparable to the energy barrier of magnetic anisotropy, i.e., up to temperature so-called the blocking temperature, T_B. The difference between ZFC and FC measurements is that the cooling sample in a magnetic field leads to freezing magnetic moments of nanoparticles according to the direction of applied fields. This means that the FC magnetization has a maximum value at lowest temperature studied and decreases gradually with increasing temperature up to T_B. Above T_B, nanoparticles of both ZFC and FC processes relax at the same frequency, therefore they exhibit the same magnetization values.

The 100 Oe magnetization data for the samples 1, 2, 3 and austenitic steel 316L appear to be quite similar to those measured in the lower field of 10 Oe. However, a quantitative comparison of the 10 and 100 Oe data divulges essential difference in the T_{max} and T_{ir} positions, which are shifted to lower values with increasing applied field strength. This behavior can be explained in superparamagnetic relaxation model since the blocking temperatures of nanoparticles are expected to decrease due to the reduction in the energy barrier by the magnetic field. The behavior of sample 5 deviates from those of the remaining, and this is certainly related to ferromagnetic ordering of Fe_2B at a higher temperature than room temperature. The T_{max} and T_{ir} values observed by 10 and 100 Oe measurements on the doped samples 1 – 4 are gathered in **Table. 2**.

Table 2. Temperature T_{max} [K] of samples 1, 2, 3, and 4, and austenitic steel 316L and the irreversibility temperature T_{ir} [K] of samples 1, 2, 3, and 4 in magnetic fields of 10 and 100 Oe.

	Magnetic field	sample 1	sample 2	sample 3	sample 4	Austenitic Steel 316L
T_{max}	10 Oe	140±10	140±10	180±10	--	31 ± 5
	100 Oe	71 ±10	110±10	150±10	92 ±10	31 ± 5
T_{ir}	10 Oe	200±10	210±10	280±10	---	
	100 Oe	130±10	150±10	210±10	180±10	

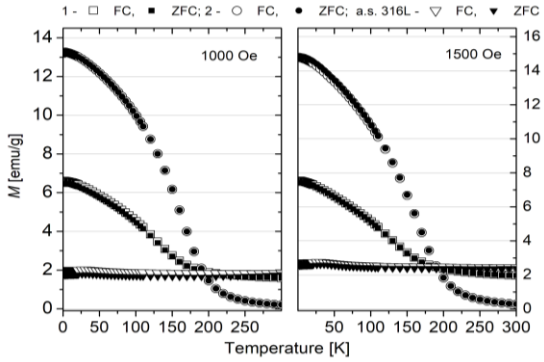

Fig. 6. Magnetization measured with FC and ZFC modes for the samples 1, 2 and austenitic steel 316L in magnetic fields 1000 Oe (left panel) and 1500 Oe (right panel).

High magnetic field properties

High-field magnetization data of the investigated samples are shown in **Fig. 6**. Clearly, the temperature dependencies of the high-field magnetization of the doped samples are markedly different from those measured in low fields. Instead of thermomagnetic irreversibility ($M_{FC}(T)>M_{ZFC}(T)$) below T_{ir} presented above, we perceive that the magnitudes of high-field $M_{FC}(T)$ in the studied temperature range are comparable to those of $M_{ZFC}(T)$. The field-induced vanishing of the irreversibility in magnetization curves of superparamagnetic materials strongly implies that magnetic anisotropy of the studied systems is destroyed by an application of external fields.

Obviously, the saturation tendency of both $M_{FC}(T)$ and $M_{ZFC}(T)$ observed at low temperatures comply with very small magnetic anisotropy [35]. It is in stark contrast to the appearance of maximum in the low-field $M_{ZFC}(T)$ curves, the high-field magnetization data do exhibit an inflection point, suggesting a field-induced magnetic phase transition at T_{ord}. The value of T_{ord} can be taken as the minimum of the temperature dependence of the magnetization derivative dM(T)/dT. We observe T_{ord} = 130, 160 and 200 K for sample number x = 1, 2 and 3, respectively. It is important to emphasize that the applied fields up to 2500 Oe did not alter the position of T_{ord}.

The question as to the physical mechanism responsible for the field-induced phase transition is an interesting one, and we will go back to this issue in the section Discussion. An important observation, which requires clarification, is the low-temperature anomaly at around 20 K in the ZFC magnetization curves of the doped samples (**see Fig. 5a**). Therefore, we inspect the temperature dependence of the magnetization for the steel 316L measured in several magnetic fields. The ZFC and FC magnetization data are in agreement with those previously reported [12, 13]. Nonetheless, our results point out two features: (a) The low-temperature anomaly around 20 K in ZFC data of the doped samples originates from the steel 316L matrix, (b) The irreversibility behavior at temperatures below 300 K may be due to some phase(s) of ferromagnetic nature, for which ordering temperature is higher than 300 K.

We have measured hysteresis loops for 1, 2, 4, 5, and pure 316L samples. The magnetization saturation is reached much later by samples with higher Ti-B-C concentration, moreover, the magnetization decreases with increasing temperature. The coercive field is as high as 60 Oe, while remnant parameter about 3 emu/g. For low temperatures (~10 K) one can observe some shift in values of the coercive field (~3 Oe) and remnant parameter (~0.2 emu/g). It may suggest the presence of bias exchange interactions characteristic for core-shell system. Soares et al. [36] suggested a model, which can explain a shift of the hysteresis loop at the low magnetic field by this kind of interaction. With this aim, they have drawn dM/dH dependence versus magnetic field and presented the dependence very close to the one obtained for samples 4 and 5. In this model, it is assumed the FM core as having a single magnetic domain while the shell has a mixture of small FM and AFM regions.

The above mentioned features clearly confirm the influence of Ti-B-C content onto magnetic properties of 316L stainless steel.

Discussion

The magnetic measurements indicated that the Ti-B-C dopant has a dramatic effect on the doped composites. MS investigations supported the ferromagnetic resonance studies and their analysis. Double integral FMR intensity, χ_{EPR}, (FMR susceptibility), confirm magnetization changes in both ZFC and FC modes.

The features observed in the doped alloys can reasonably be interpreted with the superparamagnetic model, where the physical mechanism is governed by a competition of superparamagnetic relaxation due to magnetic anisotropic energy barriers and thermal relaxation. The balance of the two energetic scales happens at so-called blocking temperature T_B. Apparently, involving the superparamagnetic model, we can interpret not only the low field dependence of the ZFC and FC magnetization (data are shown in **Fig. 5a**) but also a linear change of T_{max} and T_{ir} with increasing dopant concentrations up to 7 vol. % **(Fig. 5b)**. The dependencies of T_{max} and T_{ir} vs. x are obviously consistent with the ensuant formula: $T_B = K<V>/25k_B$ predicted for superparamagnetic systems [37], where K is the first-order magneto-crystalline anisotropy constant, <V> is the average nanoparticle volume and k_B is the Boltzmann constant.

We may notice, however, that the theoretical blocking temperature T_B differs from determined T_{max} and T_{ir} values here **(Fig. 5b)**. Experimentally, the maximum observed in the ZFC magnetization curves occurs at lower temperature than T_{ir}. This behavior signalizes different distributions of particle sizes in the samples. In principle, a fraction of the largest particles freeze already at T_{ir}, whereas the major fraction becomes blocked at T_{max}. Therefore, to quantitatively characterize the magnetic behavior of any superparamagnetic system having different nanoparticle sizes, one needs also to scrutinize the distribution of the magnetic anisotropy energy barrier f(T). Taking into consideration the fact that the FC magnetization accounts for the contribution of all nanoparticles, while the ZFC magnetization refers only to the magnetization of the nanoparticles, which energy barriers are overcome by thermal energy k_BT and start to flip randomly, the distribution function f(T) can be expressed with the equation [38]:

$$M_{ZFC} = M_{FC} \int_{LT}^{HT} f(T')dT', \quad (4)$$

where LT and HT are the lowest and highest temperatures of the magnetization experiments. We estimated the anisotropy energy distribution by calculating the temperature derivative of the ratio $M_{ZFC}(T)/M_{FC}(T)$:

$$f(T) = \frac{d}{dT}\left[\frac{M_{ZFC}(T)}{M_{FC}(T)}\right]. \quad (5)$$

The maximum in the *f(T)* curves locates at 195 and 160 K, respectively, i.e., in between the T_{max} and T_{ir} values. Basically, if there are only superparamagnetic and thermal relaxations, the shape of the *f(T)* should be symmetrical. Here, we see a left-skewed distribution, which implies the presence of more than one superparamagnetic relaxation.

Bearing in mind two circumstances: i) the anisotropic energy distribution depends not only on contents of magnetic nanoparticles but also on the sizes and magnetic types of nanoparticle, and ii) for studied samples, the width values of *f(T)*-maximum are relatively large (~60 K in 10 Oe and 100 K in 100 Oe measurements), we may conjecture that different sizes and/or different magnetic types of nanoparticle dopants give a rise to the relaxation processes.

Finally, the discussion can address the question of the nature of high-field-induced magnetic phase transition shown in **Fig. 6**. In principle, even the long-rangeRuderman-Kittel-Kasuya-Yosida - type interaction exists in the doped samples, its strength is not expected to be significant, because the investigated systems contain dopants less than 10 vol % and surely the magnetic moments are too diluted. Thus, we believe that the strength long-range correlation is insufficient to give long-range ordering (LRO) of the classical type. On the other hand, the magnetic moments being arranged in a parallel, antiparallel manner or randomly at the outset can be turned collectively by applying suitable high field strengths. In this situation, local moments formed by magnetic clusters, independently of the electronic environments of the clusters, display ferromagnetic-like phase transition. One may envisage even a microscopic ordering between magnetic moments within clusters but without long-range magnetic correlations required for a true long-range magnetic order. This explanation is plausible since it is supported by the fact that the values of T_{ord} are practically insensitive to changes in applied magnetic field strengths.

Conclusions

In conclusion, we have successfully prepared composites consisting of 316L austenitic steel as matrix and nanocrystalline Ti-B-C powders up to 7 vol. % as a dopant. XRD and SEM studies on these samples revealed a homogeneous mixture of γ-Fe and magnetic $Me_{23}(C, B)_6$ (Me = Cr, Fe, and Mn) phases. The magnetic measurements indicated strong magnetic properties occurring in these doped materials, which can be characterized by an irreversibility behavior of magnetization below T_{ir} and maximum T_{max} in ZFC magnetization.

The sample history, temperature and dopant concentration dependences of the magnetization have been interpreted using the superparamagnetic model. The field-induced phase transition observed in the field above 1000 Oe is thought to be due to the flipping of magnetic moments within clusters by applied fields but without a long-range ordering. Finally, the presented results underscore also the possibility of getting new, desired properties for specific applications of the 316L steel by suitable tuning of concentrations and sizes of dopants.

A maximum of two tables are allowed and authors must choose only those table for the main manuscript which delivers main and most important information. Remaining table must be included in supplementary information.

Make sure that good quality figure with clear: (i) key messages, (ii) levels/font sizes, (iii) scales, (iv) color contrasts, (v) line widths/symbol sizes are necessary (qualifying this criteria is minimum requirement for manuscript publication irrespective of referee comments).

Author's contributions

Conceived the plan: SMK, AB; Performed the expeirments: SMK, AB, TB, GL, PF; Data analysis: SMK, AB, VHT, PF, TB, GL; Wrote the paper: SMK, VHT, AB, TB. Authors have no competing financial interests.

References

1. Tobler R.L.; Nishimura A.; Yamamoto J.;*Cryogenic*s (Guildf), **1997**, *37*, 533. **DOI:** 10.1016/S0011-2275(97)00071-4.
2. Crangle J., Fogarty A., Taylor M.J.,*J. Magn. Magn. Mater*.,**1992**, 111, 255. **DOI:** 10.1016/0304-8853(92)91084-7.
3. Manjanna J., Kamada Y., Kobayashi S., Takahashi S., Kikuchi H., *J. Appl. Phys*., **2008**, 07E713 **DOI:** 10.1063/1.2830831.
4. Fuks H., Kaczmarek S.M., Leniec G., Michalski J., Kucharska B., Wach P., *Archives of Metallurgy and Materials*, in the print
5. SiegelR.W., *Nanostruct. Mater*.,**1993**, 3, 1.
6. Gleiter H., Prog. *Mater. Sci*.,**1989**, 33, 223.
7. Gryaznov V.G., Trusov L.I., *Prog. Mater. Sci*., **1993**, 37, 289.
8. Dormann J., Fiorani D., Magnetic Properties of Fine Particles, North-Holland, Amsterdam **1992**.
9. R.D. Shull, *IEEE Trans. Magn*., **1993**, 29, 2614.
10. Shull R.D., McMichael R.D., Ritter J.J., Schwartzendruber L.J., Bennett L.H., in: *Proc. 7th Int. Cryocoolers Conf*., Ed. M. Stoyanof, New Mexico **1993**, p. 1133.
11. R.F. Ziolo, E.P. Giannelis, B.A. Weinstein, M.P. O'Horo, B.N. Ganguly, V. Mehrotra, M.W. Russell, D.R. Huffman, *Science*, **1992**, 257, 219.
12. Anton I., de Sabata I., Vékás L., *J. Magn. Magn. Mater*., **1990**, 85, 219.
13. Raj K., Moskowitz B., Casciari R.J., *J. Magn. Magn. Mater*.,**1995**, 149, 174. **DOI:** 10.1016/0304-8853(95)00365-7
14. Biedunkiewicz A., Figiel P., Biedunkiewicz W., Grzesiak D., *Chem. List*.,**2011**, 105, 773. **DOI:** http://www.chemicke-listy.cz/docs/full/2011_s5_s767-s780.pdf
15. Guskos N., Typek J., Bodziony T., Zolnierkiewicz G., Maryniak M., Biedunkiewicz A., *J. Alloys Comp*., **2009**, 470, 51. **DOI:** 10.1016/j.jallcom.2008.03.029
16. Guskos N., Bodziony T., Maryniak M., Typek J., Biedunkiewicz A., *J. Alloys Comp*. **2008**, 455, 52 **DOI:** 10.1016/j.jallcom.2007.01.071
17. Guskos N., Bodziony T., Biedunkiewicz A., Aidinis K., *Acta Phys. Pol. A*,**2005**, 108, 311. **DOI:** 10.12693/APhysPolA.108.311
18. Bodziony T., Guskos N., Biedunkiewicz A., Typek J., Wróbel R., Maryniak M., *Mater. Sci.-Poland*, **2005**, 23, 899.
19. Figiel P., Biedunkiewicz W., Grzesiak D., *J. Therm. Anal. Calorim*., **2012**, 108, 979. **DOI:** 10.1007/s10973-011-2012-9
20. Degnan C.C., Shipway P.H., *Wear*, **2002**,252, 832. **DOI:** 10.1016/S0043-1648(02)00051-0
21. Zavareh M.A., Aly A., Mohammed D., Roudan M.A., A. Zavareh, *Int. J. Innov. Res. Sci. Eng*., **2014**, 2, 294. **DOI:** http://ijirse.in/docs/May14/IJIRSE140504.pdf
22. Khanra A.K., *Bull. Mater. Sci*., **2007**, 30, 93. **DOI:** 10.1007/s12034-007-0016-7
23. Thevenot F., *J. Eur. Ceram. Soc*., **1990**, 6, 205. **DOI:** 10.1016/0955-2219(90)90048-K
24. Sinha A., Mahata T., Sharma B.P., *J. Nucl. Mater*., **2002**, 301, 165. **DOI:** 10.1016/S0022-3115(02)00704-3
25. Pei L.Z., Xiao H.N., *J. Mater. Process. Technol*., **2009**, 209, 2122. **DOI:** 10.1016/j.jmatprotec.2008.05.003
26. Far S.H.E., Davoodi A., *J. Cent. South Univ.*,2017, 24, 1. **DOI:** 10.1007/s11771-017-3402-3
27. Yin Y., Zhang W., Dong L., Lei Y., Li J., Xiao L., *Adv. Mater. Res*., **2009**, 79–82, 1991. **DOI:** 10.4028/www.scientific.net/AMR.79-82.1991.
28. Yang Y.-F., Wang H.-Y., Zhao R.-Y., Liang Y.-H., Jiang Q.-C., *Int. J. Appl. Ceram. Technol*., **2009**, 6, 437. **DOI:** 10.1111/j.1744-7402.2008.02282.x.
29. Biedunkiewicz A., Figiel P., Gabriel U., Sabara M., Lenart S., *Cent. Eur. J. Phys*., **2011**, 9(2), 417. **DOI:** 10.2478/s11534-010-0121-x.
30. Scherrer P., *Math. Klasse*.,**1918**, 98–100. **DOI:** 10.1007/978-3-662-33915-2.
31. Rondinone A.J., Samia A.C.S., and Zhang Z.J., *J. Phys. Chem. B*,**1999**, 103, 6876. **DOI:** 10.1021/jp9912307
32. Néel L., *Ann. Geophys*., **1949**, 5, 99.
33. Néel L., Oeuvres Scientifique de Louis Néel. Centre national de la RechercheScientifique, **1978**
34. Stoner E.C., and WohlfarthE.P..*Philos. Trans. R. Soc*. London, Ser. A, **1948**, 240, 599.
35. Bitoh T., Ohba K., Takamatsu M., Shirane T., Chikazawa S., *J.Phys. Soc. Japan.*, **1995**, 64, 1305. **DOI:** 10.1143/JPSJ.64.1305.
36. Soares J.M., Conceição O.L.A., Machado F.L.A., Prakash A., Radha S., Nigam A.K., *J. Magn. Magn. Mater*,**2015**, 374,192. **DOI:** 10.1016/j.jmmm.2014.08.015
37. Néel L., *C. R. Acad. Sci*., **1949**, 228, 664
38. Néel L., *CR Acad. Sci.* Paris, **1949**, 228.664: 195

(e) Meeting/Conference/Symposium Abstract:

5. Larcher, D. Abstracts of Paper, Session S2: Lithium-ion Batteries, Symposium S, Mater. Res. Soc. Symp. Proc. 822, Warrendale, PA, *Vol. 822*, **2004**.

